Driving and detecting topological phase transition in noncentrosymmetric systems via an all-optical approach

Mengtong Yang,[1] Xiaoyan Miao,[1] Si Li,[1] Jian Zhou [ORCID],[2,*] and Chunmei Zhang [ORCID][1,†]

[1]*School of Physics, Northwest University, Xi'an 710127, China*
[2]*Center for Alloy Innovation and Design, State Key Laboratory for Mechanical Behavior of Materials,*
Xi'an Jiaotong University, Xi'an 710049, China

The use of strong periodic light irradiation to drive Bloch state evolution and another weak light to probe this dynamic process is an effective yet underexplored strategy. Here, based on the first-principles calculations and Floquet theory, we systematically study the electronic structure evolution in a noncentrosymmetric system under a circularly polarized pump light. This process is analyzed using the Bernevig-Hughes-Zhang model, in which we elucidate that the pump light renormalizes the hopping integral and acts as an effective spin-orbit coupling, so that it reduces the system band gap. Using a monolayer BiSb as an exemplary material platform, we show that its band gap would close and reopen as the pump light intensity increases, corresponding to a topological phase transition (TPT) with distinct Chern numbers. We further propose that a weak probe light could capture such a TPT through second-order nonlinear optical responses, such as the bulk photovoltaic effect (BPVE) and second harmonic generation (SHG) process. Both the BPVE and SHG are largely enhanced in the Floquet-induced topologically nontrivial state. Importantly, the shift current flips direction under the TPT, offering an exquisite characteristic tool with high sensitivity to characterize the Chern number. Our work proposes an all-optical strategy to pump and probe the TPT in noncentrosymmetric systems, providing potential design strategy of dynamic nonlinear optical devices.

I. INTRODUCTION

Electronic band engineering has been one of the main targets for electrical transport, information processing, energy storage and conversion, etc. It is typically done in semiconductors by changing their chemical composites or applying structural deformations (e.g., elastic strain engineering). In addition to these chemical or mechanical approaches, optical control on the electronic band structure and even band topology has become a promising and attractive strategy during the past decade. Optical approaches are advantageous owing to their noninvasive nature. They could largely reduce foreign atom introduction and are less susceptible to lattice damage. Most optical responses, e.g., optical conductance, light absorption and reflection, second harmonic generation (SHG), and photoelectric conversion, are all based upon band dispersion, note that the all-optical pump and probe technique is realized in photonic lattice or optical fiber [1–3], but the optical control of the electronic band structure is still at its nascent stage in condensed matter physics. It would be intriguing to develop all-optical read/write schemes for electronic devices so that it could aid in development of novel technologies and material platforms with fast kinetics, good controllability, and high tunability.

Floquet engineering is a powerful tool that could modulate the electronic band structure in an athermal and noncontacting way [4]. When a system is irradiated by a monochromatic light, its time-dependent Hamiltonian satisfies $H(t + T) = H(t)$ with periodicity $T = \frac{2\pi}{\Omega}$, where Ω is the angular frequency of the driving field. Similar to the Bloch theorem that applies in real space, this time-periodic field also modulates the electronic dispersion relation. As such, the electronic Bloch states transform into the Floquet-Bloch states. This dynamic electronic renormalization process has been realized and observed in various materials, i.e., bulk black phosphorus [5], two-dimensional (2D) monolayer transition metal dichalcogenide [6], Bi [7], graphene [8], FeSe superconductor [9], etc. Such nonequilibrium optical engineering evokes several intriguing physical processes such as phase changes [10–12], photocarrier density modulation [13], and topological phase transitions (TPTs) [14,15]. In particular, the TPT that switches the topological index has been predicted to be useful for various cutting-edge technologies, such as quantum computing and quantum information devices, with low energy consumption and limited energy dissipation.

During the past decade, various materials with nontrivial band topology have been extensively studied, and usually exhibit quantized electrical conductance such as quantum spin Hall effect and quantum anomalous Hall effect. The optical method to probe such band topology variation is still underexplored. Very recently, it has been theoretically proposed that nonlinear optical (NLO) approaches [e.g., bulk photovoltaic

effect (BPVE), SHG, and nonlinear Hall effect] are closely related to the geometric Berry phase of the electronic wave function [16,17]. Therefore, it is desirable to explore an all-optical control and detection method for TPTs.

In this work, we perform density functional theory (DFT) calculations to illustrate such an approach in a noncentrosymmetric 2D material, BiSb monolayer. The BiSb compound with a hexagonal layered structure has been fabricated long ago [18], and its single-layer form can be exfoliated [19]. Note that the ultrahigh surface-to-volume ratio of 2D materials guarantees their good optical accessibility and limited light absorption. Hence, the light induced heating problem can be largely reduced. Without light irradiation, it exhibits a direct band gap (0.37 eV) with its valence band maximum and conduction band minimum locating at Γ. This band gap can effectively reduce under circularly polarized light (CPL) irradiation through the Floquet band-engineering process. At a critical light intensity, the material experiences a normal insulator to nontrivial Chern insulator (Chern number of ± 1, depending on the pump CPL handedness) phase transition. In order to probe such a transition, we propose to apply another weak light to induce second order nonlinear BPVE and SHG. Our calculations suggest that both of them are significantly enhanced after the TPT (Chern number of ± 1). In particular, the topologically related shift current generation flips its flowing direction across the TPT, serving as an exquisite characteristic tool with high sensitivity to characterize the Chern number. This suggests an all-optical approach to trigger and detect TPTs for optoelectronic applications.

II. METHODS

A. Density functional theory

The DFT calculations are performed in the Vienna *ab initio* simulation package (VASP) [20–22], using the projector augmented-wave (PAW) method [23] in PSLIBRARY [24]. The exchange-correlation interaction is treated by the Perdew-Burke-Ernzerhof (PBE) functional [25], and a plane-wave basis set with a cutoff energy of 500 eV is used to expand the valence electrons. A vacuum space of over 15 Å along the z direction is added to eliminate the artificial layer interactions. The first Brillouin zone integration is sampled by Γ-centered Monkhorst-Pack k-point meshes [26] with a grid of $11 \times 11 \times 1$. The van der Waals interaction is described by the DFT-D3 method [27]. The spin-orbit coupling (SOC) is included self-consistently throughout all the calculations. We use the WANNIER90 code [28,29] to construct its tight-binding Hamiltonian. In order to explore the dynamic stability, phonon dispersion is calculated through the finite displacement method [30], as implemented in the PHONOPY code [31]. The *ab initio* molecular dynamics simulations are carried out in a canonical ensemble using the Nosé-Hoover heat bath scheme [32].

B. Band theory of bulk photovoltaic effect

Bulk photovoltaic effect contains shift current and injection current generation. Under alternating electric field E at frequency ω, the linearly polarized light (LPL) induces normal shift current [$\sigma^{abb}(0; \omega, -\omega)$] and magnetic injection current

[$\eta^{abb}(0; \omega, -\omega)$] photoconductances, which are evaluated via [33–35]

$$\sigma^{abb}(0; \omega, -\omega) = \frac{\pi e^3}{\hbar^2} \int \frac{d\mathbf{k}}{(2\pi)^3} \sum_{m,n} f_{mn} R_{mn}^{a;b} |r_{mn}^b|^2 \delta(\omega_{nm} - \omega), \tag{1}$$

$$\eta^{abb}(0; \omega, -\omega) = -\frac{\tau \pi e^3}{2\hbar^2} \int \frac{d\mathbf{k}}{(2\pi)^3}$$
$$\times \sum_{m,n} f_{mn} \Delta_{mn}^a |r_{mn}^b|^2 \delta(\omega_{nm} - \omega). \tag{2}$$

Here, LPL is polarized along the b direction. $f_{mn} = f_m - f_n$ is the Fermi-Dirac occupation difference between band m and n, $r_{mn}^b = i\langle m|\partial_{k_a} n\rangle$ is the interband Berry connection, $R_{mn}^{a;b} = \partial_a \phi_{mn}^b - A_{mm}^a + A_{nn}^a$ is the shift vector, and ϕ_{mn}^b is the phase of $r_{mn}^b = |r_{mn}^b| e^{i\phi_{mn}^b}$. $R_{mn}^{a;b}$, being a gauge invariant quantity, has the unit of length and can be physically interpreted as a position change of the wave packet during interband transition between valence and conduction bands. $\Delta_{mn}^a = v_{mm}^a - v_{nn}^a$ measures the band velocity difference during excitation. The $|r_{mn}^b|^2 \delta(\omega_{nm} - \omega)$ evaluates absorption rate according to Fermi's "golden rule." The broadening factor of the delta function is adopted to be 0.02 eV.

Equation (2) is equivalent to the contribution from quantum metric tensor $g_{mn}^{bb} = \sum_{\mu, \upsilon} \text{Re}\{r_{m_\upsilon n_\mu}^b r_{n_\mu m_\upsilon}^b\}$, where μ, υ represent the degenerate bands arising from the potential Kramers degeneracy (e.g., in antiferromagnetic configurations) [36],

$$\eta^{a,bb}(0; \omega, -\omega) = -\frac{\tau \pi e^3}{2\hbar^2} \int \frac{d\mathbf{k}}{(2\pi)^3} f_{mn} \Delta_{mn}^a (2g_{mn}^{bb})$$
$$\times \delta(\omega_{nm} - \omega). \tag{3}$$

Accordingly, the magnetic injection current arises from an excitation between m and n, where g_{mn}^{bb} is weighted by the asymmetric group velocity difference Δ_{mn}^a at the time-reversed $\pm\mathbf{k}$ pairs. The $\Delta_{mn}^a g_{mn}^{bb}$ is quantum metric dipole [36–39].

C. Second harmonic generation susceptibility

According to the band theory, the SHG susceptibility is evaluated by [40–43]

$$\chi_{abc}^{(2)}(-2\omega; \omega, \omega) = \chi_{\text{II}}^{abc}(-2\omega; \omega, \omega) + \eta_{\text{II}}^{abc}(-2\omega; \omega, \omega)$$
$$+ \sigma_{\text{II}}^{abc}(-2\omega; \omega, \omega). \tag{4}$$

The first term in Eq. (4) denotes the interband contribution,

$$\chi_{\text{II}}^{abc}(-2\omega; \omega, \omega) = \frac{e^3}{\hbar^2} \sum_{nml} \int \frac{d\mathbf{k}}{(2\pi)^3} \frac{r_{nm}^a \{r_{ml}^b r_{ln}^c\}}{\omega_{ln} - \omega_{ml}}$$
$$\times \left(\frac{f_{ml}}{\omega_{ml} - \omega} + \frac{f_{ln}}{\omega_{ln} - \omega} + \frac{2f_{nm}}{\omega_{mn} - 2\omega} \right), \tag{5}$$

where

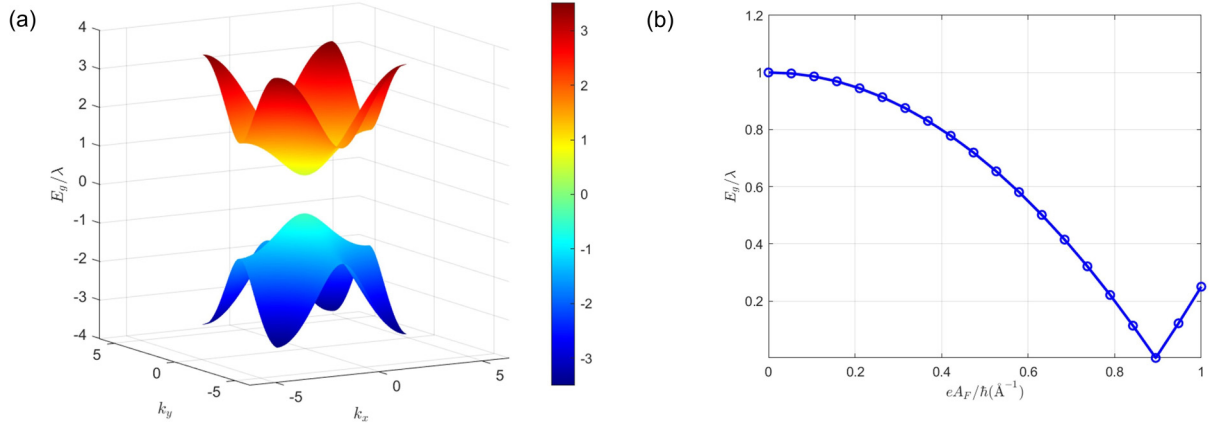$$\{r_{ml}^b r_{ln}^c\} \equiv \frac{1}{2}(r_{ml}^b r_{ln}^c + r_{ml}^c r_{ln}^b). \tag{6}$$

FIG. 1. (a) Band dispersion (near band edge) for the BHZ model ($A_F = 0$, we set $e = \hbar = 1$). (b) Band-gap variation as A_{F} is increased, showing a clear quadratic reduction. Here we set $M = -1.5\lambda$ and $\hbar\Omega = 8\lambda$.

The second term in Eq. (4) is intraband contribution,

$$\eta_{\mathrm{II}}^{abc}(-2\omega;\omega,\omega) = \frac{e^3}{\hbar^2} \int \frac{d\mathbf{k}}{(2\pi)^3} \left\{ \sum_{nml} \omega_{mn} r_{nm}^a \{r_{ml}^b r_{ln}^c\} \left(\frac{f_{nl}}{\omega_{ln}^2(\omega_{ln} - \omega)} + \frac{f_{lm}}{\omega_{ml}^2(\omega_{ml} - \omega)} \right) - 8i \sum_{nm} \frac{f_{nm} r_{nm}^a}{\omega_{mn}^2(\omega_{mn} - 2\omega)} \{\Delta_{mn}^b r_{mn}^c\} \right.$$
$$\left. - \frac{2 \sum_{nml} f_{nm} r_{nm}^a \{r_{ml}^b r_{ln}^c\}(\omega_{ln} - \omega_{ml})}{\omega_{mn}^2(\omega_{mn} - 2\omega)} \right\}. \tag{7}$$

The modification term is

$$\sigma_{\mathrm{II}}^{abc}(-2\omega;\omega,\omega) = \frac{e^3}{2\hbar^2} \int \frac{d\mathbf{k}}{(2\pi)^3} \left\{ \sum_{nml} \frac{f_{nm}}{\omega_{mn}^2(\omega_{mn} - \omega)} \left[\omega_{nl} r_{lm}^a \{r_{mn}^b r_{nl}^c\} - \omega_{lm} r_{nl}^a \{r_{lm}^b r_{mn}^c\} \right] + i \sum_{nm} \frac{f_{nm} r_{nm}^a \{\Delta_{mn}^b r_{mn}^c\}}{\omega_{mn}^2(\omega_{mn} - \omega)} \right\}. \tag{8}$$

Note that in all above equations [Eqs. (1)–(8)], integrals in the whole Brillouin zone are performed. In the three-dimensional (3D) periodic boundary condition, this corresponds to dividing the k-weighted integrands by the total unit cell volume, which contains the lattice constant along z (denoted to be L_z). In order to provide susceptibility values in the conventional 3D unit system, we multiply a factor of $\frac{L_z}{d_{\mathrm{eff}}}$, where d_{eff} refers to effective thickness of the BiSb monolayer (~ 0.2 nm).

III. RESULTS

A. Floquet band engineering on the Bernevig-Hughes-Zhang model

Before studying a realistic material, we start our discussion using the well-known 2D Bernevig-Hughes-Zhang (BHZ) model [44], which was introduced to describe the TPT in the HgTe quantum well. Before the pump CPL is introduced, the intact Hamiltonian near the band edge is [in the basis set of ($|e_\uparrow\rangle, |h_\uparrow\rangle, |e_\downarrow\rangle, |h_\downarrow\rangle$), where e and h denote electron and hole, respectively]

$$H_0(\mathbf{k}) = (M + \lambda \cos k_x + \lambda \cos k_y)\sigma_0\tau_z + \lambda \sin k_y \sigma_0 \tau_y$$
$$+ \lambda \sin k_x \sigma_z \tau_x, \tag{9}$$

where σ and τ are Pauli matrices that apply on the spin and carrier (electron or hole) degrees of freedom, respectively. M characterizes the band topology and λ denotes the effective

hopping. Here, we take $M = -1.5\lambda$, which corresponds to a trivial semiconductor without band inversion. The schematic band structure is plotted in Fig. 1(a). It has a direct band gap of $2 \times |M + 2\lambda|$.

When the pump CPL is turned on, we can apply the perturbation theory to conduct the Floquet band engineering process [45–47]. The vector potential of light enters the momentum parameter via Peierls substitution, $\mathbf{k} \rightarrow \mathbf{k} + \frac{e}{\hbar}\mathbf{A}(t)$. We assume a normal incidence condition (light propagating along z). The vector potential of light takes the form $\mathbf{A}(t) = A_F(\cos \Omega t, \eta \sin \Omega t, 0)$, where $\eta = +1$ (-1) denotes the left (right)-handed CPL. A_F is the vector potential amplitude with $eA_{\mathrm{F}}/\hbar$ in unit of Å^{-1}. According to the van Vleck expansion [48,49], the light-dressed Hamiltonian can be evaluated by

$$H_F(\mathbf{k}) \simeq \tilde{H}^0 + \sum_m \frac{[\tilde{H}^{-m}, \widetilde{H}^m]}{m} \hbar\Omega. \tag{10}$$

Here, $[\tilde{H}^{-m}, \tilde{H}^m] = \tilde{H}^{-m}\tilde{H}^m - \tilde{H}^m\tilde{H}^{-m}$ is the commutator symbol. We omit the $m \geqslant 2$ terms when $\hbar\Omega$ is sufficiently larger than the band energy region. This is also verified by our test calculations in the Supplemental Material [50]. The $\tilde{H}^q$ are the qth ($q = \pm m$) Fourier transformation components of the time-dependent Hamiltonian

$$\tilde{H}^q = \frac{1}{T} \int_0^{T=2\pi/\Omega} dt\, e^{iq\Omega t} H_0\left(\mathbf{k} + \frac{e}{\hbar}\mathbf{A}(t)\right). \tag{11}$$

It can be shown that the CPL pump light effect is twofold (for a detailed derivation, see the Supplemental Material [50]): (1) It renormalizes the hopping parameter λ, by reducing it to $\lambda[1 - \frac{1}{4}(\frac{eA_F}{\hbar})^2]$. This is irrelevant to the handedness of pump CPL. (2) The first order expansion [$m = 1$ in Eq. (10)] is proportional to $\frac{\eta\lambda^2}{\hbar\Omega}(\frac{eA_F}{\hbar})^2$, depending on the CPL chirality. These effects are analogous to previous works on a quantum ring with SOC under the LPL pump [51]. For simplicity, we focus on the band gap at the band edge, $k_x = k_y = 0$. Then, there leaves an additional term to the expanded Hamiltonian,

$$\frac{[\tilde{H}^{-1}, \tilde{H}^1]}{\hbar\Omega}\bigg|_{k=0} = -\frac{\eta\lambda^2}{\hbar\Omega}\left(\frac{eA_F}{\hbar}\right)^2 \sigma_z \tau_z. \quad (12)$$

This corresponds to the on-site intrinsic SOC interaction in various 2D materials, which is consistent with previous discussions on the antiferromagnetic FeSe monolayer [9]. Here we show that the BHZ model gives the same conclusion, suggesting its ubiquitous character. The Floquet-Bloch band quasienergies of the ($|e_\uparrow\rangle, |h_\uparrow\rangle, |e_\downarrow\rangle, |h_\downarrow\rangle$) states then become $\varepsilon(e_\uparrow) = M + 2\lambda - (\frac{\lambda}{2} + \frac{\eta\lambda^2}{\hbar\Omega})(\frac{eA_F}{\hbar})^2$, $\varepsilon(h_\uparrow) = -M - 2\lambda + (\frac{\lambda}{2} + \frac{\eta\lambda^2}{\hbar\Omega})(\frac{eA_F}{\hbar})^2$, $\varepsilon(e_\downarrow) = M + 2\lambda - (\frac{\lambda}{2} - \frac{\eta\lambda^2}{\hbar\Omega})(\frac{eA_F}{\hbar})^2$, and $\varepsilon(h_\downarrow) = -M - 2\lambda + (\frac{\lambda}{2} - \frac{\eta\lambda^2}{\hbar\Omega})(\frac{eA_F}{\hbar})^2$. Thus, at finite A_F, the degeneracy of $|e_\uparrow\rangle$ and $|e_\downarrow\rangle$ (or $|h_\uparrow\rangle$ and $|h_\downarrow\rangle$) lifts (broken time-reversal symmetry). When $\eta = 1$ (left-handed CPL), the $|e_\uparrow\rangle$ and $|h_\uparrow\rangle$ are the lowest conduction band and highest valence band, respectively. For $\eta = -1$ (right-handed CPL), they become $|e_\downarrow\rangle$ and $|h_\downarrow\rangle$. The band gap yields $E_g|_{k=0} = 2M + 4\lambda - (\lambda + \frac{2\lambda^2}{\hbar\Omega})(\frac{eA_F}{\hbar})^2$, regardless of CPL handedness. As A_F enhances, the band gap decreases quadratically. This is consistent with our numerical calculations over the entire Brillouin zone [Fig. 1(b)]. At a critical light intensity, the band gap closes and reopens, suggesting a TPT feature. This leads to a nonzero Chern number ($|C| = 1$). The contrast chirality of pump CPL yields opposite Chern number. Note that in this model discussion, we omit the Rashba or Dresselhaus type SOC effect, which would not affect the main conclusion.

B. Geometric structure and stability of BiSb monolayer

Next, we illustrate the above physical picture in a realistic material, BiSb monolayer. The bulk BiSb has a layered structure crystallized in hexagonal form [18], with the space group of $R3m$ (no. 160). When it is exfoliated into a single layer form, it belongs to the layer group [52] of $p3m1$ (no. 69), which lacks the inversion symmetry [Figs. 2(a) and 2(b)]. According to our calculations, the optimized lattice constant is 4.23 Å, and the atomic structure exhibits a puckered honey-comb lattice, which agree well with the previous results [19]. The dynamic stability of monolayer BiSb is revealed by its phonon spectra (Fig. S1 of the Supplemental Material [50]), where no imaginary frequencies can be observed throughout the first Brillouin zone. We also perform *ab initio* molecular dynamics simulations at 300 and 500 K, lasting for 10 ps with a time step of 1 fs (Fig. S1). No evidence of structural destruction or lattice distortions can be observed, suggesting its good thermal stability.
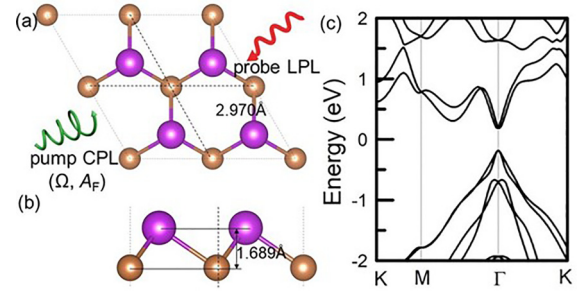

FIG. 2. (a) Top and (b) side view of a ($2 \times 2 \times 1$) supercell of BiSb monolayer. In an all-optical control scheme, the system is pumped by CPL (with angular frequency Ω and light intensity denoted by A_F), which renormalizes its band dispersion. Such Floquet-Bloch state is probed by a weak LPL (with angular frequency denoted as ω) that generates observable NLO signals. The numbers denote bond length in (a) and height of buckling in (b). (c) Calculated band structure of BiSb monolayer including full SOC effect.

C. Floquet engineered topological phase transition under circularly polarized light pump

According to our calculations with full SOC effects, the BiSb monolayer is a topologically trivial semiconductor with a direct band gap of 0.37 eV [Fig. 2(c)], consistent with previous works [53]. In comparison, we plot the band structure without SOC in Fig. S2, [50] giving a direct band gap of 0.96 eV. This indicates that strong SOC strengths in both Bi and Sb elements significantly reduce the band gap, which is beneficial for Floquet-engineered TPTs (band gap closes and reopens).

To investigate the time-dependent dynamic control of its electronic structure, we use CPL as the pump light, which breaks the time-reversal symmetry. Here we choose a photon energy of $\hbar\Omega = 8$ eV, which is much larger than the electronic band energy range of interest. Hence, one can eliminate the strong direct photon absorption as it belongs to the transparent frequency regime. In Fig. 3, the band structure with A_F ranging 0–0.6 Å^{-1} is plotted. One observes a striking band renormalization near the Fermi level. The expectation value of spin z $\langle S_z \rangle$ of each state is also given in Figs. 3(a)–3(c), while their $\langle S_x \rangle$ and $\langle S_y \rangle$ results are shown in Fig. S3 [50]. As the (right-handed) light intensity increases, the spin-up channel composes the top valence band and bottom conduction band. This is consistent with our previous BHZ model analysis. At a critical light intensity of $A_F = 0.5$ Å^{-1}, the band gap closes. This critical field strength corresponds to the peak intensity of $\sim 2 \times 10^{14}$ W/cm^2, which is achievable experimentally. Stronger light further reopens the band gap, indicating a topologically nontrivial band character. This is demonstrated by evaluating the z-component Berry curvature in occupied bands, $\mathfrak{B}_{nk}^z = i\langle\nabla_k\tilde{u}_{nk}| \times |\nabla_k\tilde{u}_{nk}\rangle$ (where $|\tilde{u}_{nk}\rangle$ is the Floquet-Bloch wave function), as plotted in Fig. 3(d). We integrate the Berry curvature in the whole 2D Brillouin zone, yielding a Chern number of 1. Therefore, these results suggest that Floquet engineering could drive distinct TPTs between normal and quantum anomalous insulating phase.

If the left-handed CPL is used, one sees that the band-gap variation [Figs. 3(e)–3(g)] is the same as the right-handed CPL case. Actually, as the intact system is $\mathcal{T}$ invariant, different
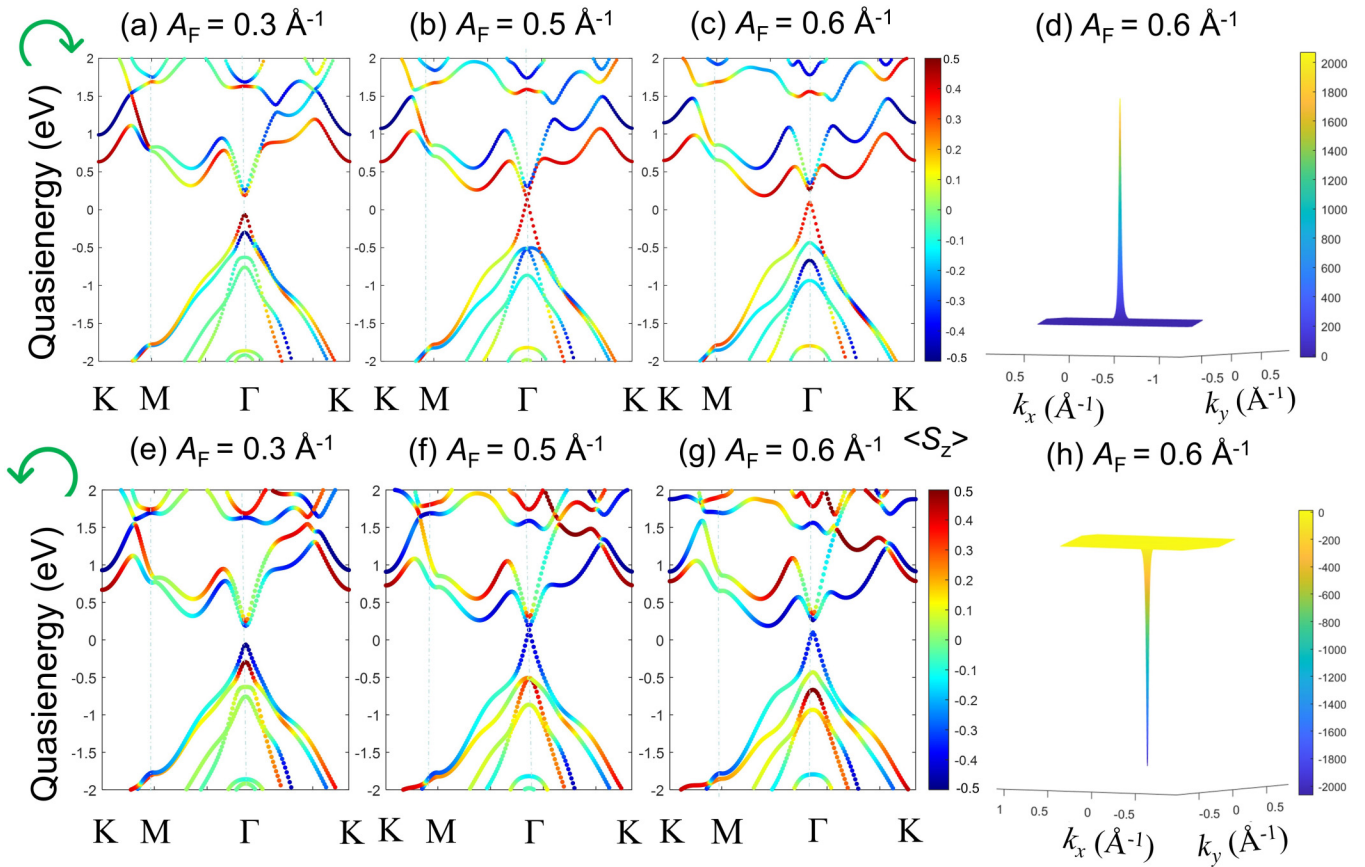
FIG. 3. The band structure evolution of BiSb monolayer under right-handed Floquet CPL (a)–(c) and left-handed Floquet CPL (e)–(g). A_F denotes the amplitude of the vector potential ($e = \hbar = 1$). The curved green arrows denote CPL chirality. The color map shows spin-z expectation value. (d),(h) k-resolved Berry curvature $\mathfrak{B}^z_{nk}$ distribution in the first Brillouin zone with $A_F = 0.6$ Å^{-1} for bands of panels (c) and (g), respectively. The color maps are in unit of Å^2.

handedness pump light corresponds a time-reversal pair with respect to each other. One then expects that the $\langle S_z \rangle$ distribution is reversed. As such, after TPTs, the Berry curvature reverses its sign, giving an opposite Chern number ($C = -1$). The positive and negative Chern numbers indicate opposite circulation direction of chiral edge modes. This provides an effective optical scheme to control the sign of the Chern number and the chirality of the quantum anomalous Hall phase [54].

D. Bulk photovoltaic effect under Floquet engineering

The topological nature is closely related to NLO responses such as BPVE and SHG in noncentrosymmetric systems [55,56]. While most previous works focus on the relationship between the Z_2 TPT (by mechanical or electrical schemes) and the BPVE, we here explore the Floquet engineering Chern number related TPT. For simplicity, we consider LPL induced NLO responses, which serve as a probe light.

Before numerical calculation, we perform symmetry analysis on the BPV generation. As the intrinsic BiSb monolayer is nonmagnetic without inversion symmetry, the LPL will induce shift current (usually dubbed normal shift current) that is scaled by shift vector and light absorbance. This can be understood by investigating the C_{3v} point group character. In this point group, the in-plane electric field follows

linear function representation, namely E. Hence, the second order in-plane electric field transforms as $E \otimes E = A_1 \oplus A_2 \oplus E$. This can be divided into symmetric and antisymmetric parts. The LPL incident light follows the symmetric representation, $\Gamma^s_{EE^*} = A_1 \oplus E$ (the antisymmetric part A_2 describes circularly polarized light). Thus, the shift current generation follows $\Gamma = \Gamma_J \otimes \Gamma^s_{EE^*} = E \otimes (A_1 \oplus E) = A_1 \oplus A_2 \oplus 2E$, giving one nonvanishing independent component (A_1). One can show that the symmetrically allowed in-plane shift current photoconductance components are $\sigma^{yyy}(\omega) = -\sigma^{yxx}(\omega)$, where ω represents the incident LPL photon frequency. In Fig. 4(a) we plot the calculated $\sigma^{yyy}(\omega)$. Without the $\Omega = 8$ eV pump (intrinsic case, $A_F = 0$), the shift current photoconductance $\sigma^{yyy}(\omega)$ has a small magnitude (within $10\,\mu A/V^2$). As the Floquet pump light intensity enhances (from $A_F = 0$ Å^{-1} to 0.4 Å^{-1}), the first dominant peak of the $\sigma^{yyy}(\omega)$ moves to lower frequency (redshift), and its magnitude keeps increasing and reaches $\sim 400\,\mu A/V^2$ at $A_F = 0.4$ Å^{-1}. This is in accordance with the band-gap reduction, which mainly dominates the interband transition. The shift current magnitude is inversely proportional to the band-gap value. During the whole process, the $\sigma^{yyy}(\omega)$ remains negative at its first peak.

It would be intriguing to see how BPV current evolves from the normal to quantum anomalous Hall insulating phase. At $A_F = 0.6$ Å^{-1}, σ^{yyy} flips its sign with a peak of
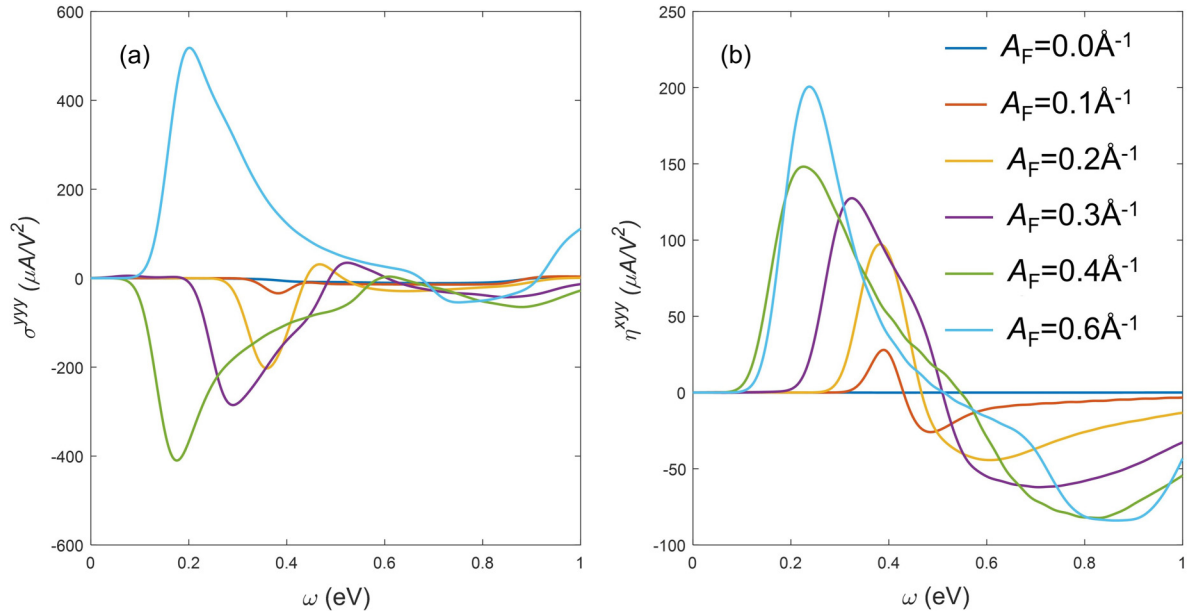
FIG. 4. The calculated (a) shift current and (b) injection current photoconductance components under right-handed CPL pump that drives Floquet band engineering.

$500\ \mu\text{A/V}^2$ near the band edge. It infers that the shift current reverses its flowing direction across the Floquet engineered TPT (Chern number variation), giving a similar trend as in strain or gate voltage induced TPT (Z_2 number change) [57]. This can be understood by separately examining its microscopic band theory expression. The shift current is scaled by the light absorption rate $|r_{mn}^b|^2 \delta(\omega_{nm} - \omega)$ and the shift vector. One notes that the sign of the absorption rate is always positive, while under band inversion, the shift vector $R_{mn}^{a,b}$ becomes to $R_{nm}^{a,b}$, giving a sign flip.

As the intrinsic BiSb monolayer is nonmagnetic, LPL irradiation does not introduce injection current (usually dubbed magnetic injection current) as in otherwise magnetic materials. The magnetic injection current arises from quantum metric dipole between the valence and conduction bands, weighted by the asymmetric group velocity differences in the momentum space, and is odd under both $\mathcal{P}$ and $\mathcal{T}$ operations. The calculated results are plotted in Fig. 4(b). At $A_F = 0$, the injection current generation is completely zero. As demonstrated previously, the Floquet pump CPL breaks $\mathcal{T}$. In this case, the system belongs to the $3m' = C_3 \oplus C_s \mathcal{T}$ magnetic point group, so that its symmetry argument is reduced to be C_3. Our calculations show that at nonzero A_F, the injection current photoconductance η arises and increases with the CPL intensity. It flows along x, rather than y as in the shift current. Taking the right-handed pump case as an example, $\eta^{xyy}(\omega = 0.35\ \text{eV})$ reaches over $125\ \mu\text{A/V}^2$ at $A_F = 0.3\ \text{Å}^{-1}$. It should be noted that this injection current is proportional to the carrier lifetime τ which strongly depends on the sample quality, electron-phonon coupling, temperature, and disorder level, etc. In the current case, we assume a conservable and experimentally achievable value of $\tau = 0.1$ ps. If such lifetime is elongated, for example to 0.2 ps, then the photoconductivity and injection current are also doubled.

One has to note that here we consider right-handed CPL as the pump light to trigger the Floquet band renormalization. Actually, the chirality of pump CPL would control the injection current direction (see Fig. S5 [50], which shows that the left-handed CPL pump gives opposite η), while leaving the shift current direction intact. This is consistent with the facts that the former one is $\mathcal{T}$ odd and the latter one is $\mathcal{T}$ even.

E. Second harmonic generation under Floquet engineering

Other than the BPVE, another second order optical process that has been widely explored is the SHG response. The search for materials with large second harmonic optical susceptibility has been of continuous interest since the early years of NLO study. Here, we evaluate the SHG responses under Floquet engineering. It should be noted that such ultrafast SHG probe can be observed owing to recent experimental advances [58]. We focus on the in-plane SHG components in Voigt notation. The $C_3(z)$ rotation constraints that $\chi_{11}^{(2)}(\omega) = -\chi_{12}^{(2)}(\omega) = -\chi_{26}^{(2)}(\omega)$ and $\chi_{16}^{(2)}(\omega) = \chi_{21}^{(2)}(\omega) = -\chi_{22}^{(2)}(\omega)$. The parallel and perpendicular SHG susceptibilities are reduced to the following expressions (see the Supplemental Material [50] for details) [59]:

$$\chi_{\parallel}(\omega) = \chi_{11}^{(2)}(\omega)\cos 3\theta + \chi_{16}^{(2)}(\omega)\sin 3\theta, \quad (13)$$

$$\chi_{\perp}(\omega) = -\chi_{11}^{(2)}(\omega)\sin 3\theta + \chi_{16}^{(2)}(\omega)\cos 3\theta. \quad (14)$$

Our calculated SHG components are shown in Fig. S6 [50]. Note that they are both complex functions. Even though one can experimentally measure the real and imaginary parts separately, it is more common to detect the absolute value. The absolute value of the SHG tensor $\chi_{11}^{(2)}$ and $\chi_{22}^{(2)}$ of BiSb monolayer under Floquet engineering are plotted in Figs. 5(a) and 5(b), respectively. It is seen that the $|\chi_{11}^{(2)}|$ and $|\chi_{22}^{(2)}|$
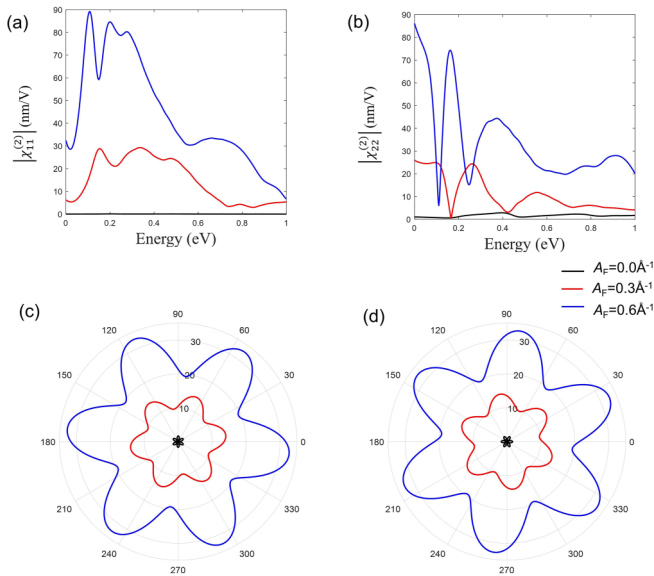
FIG. 5. The polarization-resolved SHG components (a) $|\chi^{(2)}_{11}|$ and (b) $|\chi^{(2)}_{22}|$ of BiSb monolayer under Floquet engineering with $A_F = 0$, 0.3, 0.6 Å^{-1} respectively. (c) The parallel and (d) perpendicular polar plot (as functions of probe light polarization direction) with incident photon energy $\hbar\omega = 0.6$ eV.

increase with A_F. The $|\chi^{(2)}_{ij}|$ at low incident energy increases monotonously with A_F. This is consistent with the trend that the SHG amplitude is inversely proportional to the square of transition energies. After the TPT (at the quantum anomalous Hall state), the SHG signal magnitude enhances drastically. For example, the intensity of the SHG increases sharply and reaches as high as 90 nm/V (at an incident photon energy of 0.17 eV) when $A_F = 0.6$ Å^{-1}. The giant $|\chi^{(2)}_{ij}|$ is similar to the enhanced shift current mechanism, as discussed previously [56]. Figures 5(c) and 5(d) plot the polarization-resolved parallel and perpendicular SHG responses for BiSb monolayer under Floquet engineering, at a representative incident photon energy of $\hbar\omega = 0.6$ eV. It is clear that both $\chi_\parallel$ and $\chi_\perp$ increase with A_F and keep their sixfold symmetry.

One could compare the current results with some experimentally observed SHG candidates, i.e., 3600 pm/V at the wavelength of 800 nm for TaAs [56], 350 pm/V at the wavelength of 810 nm for GaAs [60], 250 pm/V at the wavelength of 800 nm for ZnTe [61], and the 15 pm/V at the wavelength of 900 nm for BaTiO$_3$ [62]. Here, the calculated SHG component reaches the order of 10^4 pm/V in the topologically nontrivial phase, which is experimentally observable.

IV. DISCUSSION

Before concluding, we would like to make the following remarks. It is a natural question if the sample could withstand the strong pump light. In the current situation, the photon energy is much larger than the band energy of interest, which falls in the transparent frequency regime. In addition, the ultrathin nature of 2D material also reduces the potential light absorption, so that most photons would trespass through the sample. Nonetheless, the total energy flux is very strong. Note that not all absorbed photon energy will transform into

heat, which needs phonon involvements such as nonradiative electron-hole recombination. However, the direct evaluation of such a process is not straightforward, and it remains to be verified in experiments. In order to reduce potential heating problem, we propose to consider the following points: (1) The variation of the band gap under pump light is inversely proportional to photon energy, as described by the van Vleck expansion in Eq. (10). Thus, one may expect to reduce the required light electric field strength (and light intensity) using pump light with lower frequency. But one has to remember that very low Ω will make the van Vleck expansion invalid, and the physical picture would change. (2) The band gap of 2D noncentrosymmetric binary material depends on the on-site energy difference in their composing elements. The BiSb monolayer is taken as an exemplary material, and other analogous systems would exhibit a similar physical process. If one decreases its intrinsic band gap, the critical light intensity to trigger TPT can be largely reduced. (3) Note that the total energy flux scales as the time duration under light exposure. Hence, one can use laser pulses to drive the Floquet band engineering, rather than the continuous wave. Recent experiments have demonstrated that a few laser pulses are enough to realize such nonequilibrium band renormalization, which can be detected via real-time band structure characteristic techniques [63–65].

In the current work, we assume normal incidence for both pump and probe light, so that the light electric field lies in the xy plane. In principle, this is not strictly required, and nearly grazing incidence should also affect both band structure and NLO responses. However, if the light electric field contains an out-of-plane z component, the responses from the ultrathin sample would be largely limited. We argue that it is not appropriate to directly apply the current mechanism into a grazing incidence situation. Since the sample is dipolar along z, symmetry analysis suggests that light illumiation may induce out-of-plane responses. However, it corresponds to the open-circuit boundary condition theoretically, and it is the electric displacement **D** (rather than electric field **E**) that serves to be the natural variable. The potential current flowing along z also becomes the charge accumulation, which remains an open question in its definition and evaluation.

V. CONCLUSION

In conclusion, we propose an all-optical (strong CPL-pump and weak LPL-probe) technique to systematically investigate the Chern number-related TPT. This process is understood in the BHZ model. Around the TPT, the second order NLO processes, such as the shift current, injection current, and SHG susceptibility, are significantly enhanced. We find that the shift current reverses its direction across the TPT. Our system offers a realistic material platform that could host Floquet-engineered TPTs, and provides a noninvasive approach to probe it via the second order NLO. The combination of Floquet topology, inversion asymmetric, giant NLO effect, and the relationship between the TPT and NLO could generate considerable impacts in the field of dynamic nonlinearity devices, optical dynamic detector and sensor, energy harvesting and transfer, etc. Considering several recent sucessful toggles

of the Floquet engineering for electronic structure, this work would stimulate further experimental efforts and verifications.

ACKNOWLEDGMENTS

[1] B. A. Bell, K. Wang, A. S. Solntsev, D. N. Neshev, A. A. Sukhorukov, and B. J. Eggleton, Spectral photonic lattices with complex long-range coupling, Optica **4**, 1433 (2017).

[2] C. Bersch, G. Onishchukov, and U. Peschel, Experimental observation of spectral Bloch oscillations, Opt. Lett. **34**, 2372 (2009).

[3] S. Lin, L. Wang, L. Yuan, and X. Chen, All-optical control of the photonic hall lattice in a pumped waveguide array, Phys. Rev. Appl. **17**, 064029 (2022).

[4] P. S. Pershan, J. P. Van Der Ziel, and L. D. Malmstrom, Theoretical discussion of the inverse faraday effect, raman scattering, and related phenomena, Phys. Rev. **143**, 574 (1966).

[5] S. Zhou *et al.*, Pseudospin-selective floquet band engineering in black phosphorus, Nature (London) **614**, 75 (2023).

[6] Y. Kobayashi, C. Heide, A. C. Johnson, F. Liu, D. A. Reis, T. F. Heinz, and S. Ghimire, Floquet engineering of strongly driven excitons in monolayer tungsten disulfide, Nat. Phys. **19**, 171 (2023).

[7] Y. H. Wang, H. Steinberg, P. Jarillo-Herrero, and N. Gedik, Observation of floquet-bloch states on the surface of a topological insulator, Science **342**, 453 (2013).

[8] A. Bhattacharya and S. F. Islam, Photoinduced spin-Hall resonance in a k(3)-Rashba spin-orbit coupled two-dimensional hole system, Phys. Rev. B **104**, L081411 (2021).

[9] Z. F. Wang, Z. Liu, J. Yang, and F. Liu, Light-induced type-II band inversion and quantum anomalous Hall state in monolayer fese, Phys. Rev. Lett. **120**, 156406 (2018).

[10] T. Satoh, B. B. Van Aken, N. P. Duong, T. Lottermoser, and M. Fiebig, Ultrafast spin and lattice dynamics in antiferromagnetic Cr$_2$O$_3$, Phys. Rev. B **75**, 155406 (2007).

[11] M. Y. Zhang *et al.*, Light-induced subpicosecond lattice symmetry switch in MoTe$_2$, Phys. Rev. X **9**, 021036 (2019).

[12] S. Cho *et al.*, Phase patterning for ohmic homojunction contact in MoTe$_2$, Science **349**, 625 (2015).

[13] G. Sartorello, N. Olivier, J. Zhang, W. Yue, D. J. Gosztola, G. P. Wiederrecht, G. Wurtz, and A. V. Zayats, Ultrafast optical modulation of second- and third-harmonic generation from cut-disk-based metasurfaces, ACS Photon. **3**, 1517 (2016).

[14] X. Li, X. Xu, H. Zhou, H. Jia, E. Wang, H. Fu, J.-T. Sun, and S. Meng, Tunable topological states in stacked chern insulator bilayers, Nano Lett. **23**, 2839 (2023).

[15] F. Zhan, J. Zeng, Z. Chen, X. Jin, J. Fan, T. Chen, and R. Wang, Floquet engineering of nonequilibrium valley-polarized quantum anomalous Hall effect with tunable Chern number, Nano Lett. **23**, 2166 (2023).

[16] T. Morimoto and N. Nagaosa, Topological nature of nonlinear optical effects in solids, Sci. Adv. **2**, e1501524 (2016).

[17] I. Sodemann and L. Fu, Quantum nonlinear Hall effect induced by Berry curvature dipole in time-reversal invariant materials, Phys. Rev. Lett. **115**, 216806 (2015).

[18] J. P. Dismukes, R. J. Paff, R. T. Smith, and R. Ulmer, Lattice parameter and density in bismuth-antimony alloys, J. Chem. Eng. Data **13**, 317 (1968).

[19] K. Wu, J. Chen, H. Ma, L. Wan, W. Hu, and J. Yang, Two-dimensional giant tunable Rashba semiconductors with two-atom-thick buckled honeycomb structure, Nano Lett. **21**, 740 (2021).

[20] G. Kresse and J. Hafner, *Ab initio* molecular dynamics for liquid metals, Phys. Rev. B **47**, 558 (1993).

[21] G. Kresse and J. Furthmüller, Efficient iterative schemes for *ab initio* total-energy calculations using a plane-wave basis set, Phys. Rev. B **54**, 11169 (1996).

[22] P. E. Blöchl, Projector augmented-wave method, Phys. Rev. B **50**, 17953 (1994).

[23] G. Kresse and D. Joubert, From ultrasoft pseudopotentials to the projector augmented-wave method, Phys. Rev. B **59**, 1758 (1999).

[24] A. Dal Corso, Pseudopotentials periodic table: From H to Pu, Comput. Mater. Sci. **95**, 337 (2014).

[25] J. P. Perdew, K. Burke, and M. Ernzerhof, Generalized gradient approximation made simple, Phys. Rev. Lett. **77**, 3865 (1996).

[26] H. J. Monkhorst and J. D. Pack, Special points for Brillouin-zone integrations, Phys. Rev. B **13**, 5188 (1976).

[27] S. Grimme, Semiempirical GGA-type density functional constructed with a long-range dispersion correction, J. Comput. Chem. **27**, 1787 (2006).

[28] A. A. Mostofi, J. R. Yates, G. Pizzi, Y.-S. Lee, I. Souza, D. Vanderbilt, and N. Marzari, An updated version of wannier90: A tool for obtaining maximally-localised Wannier functions, Comput. Phys. Commun. **185**, 2309 (2014).

[29] A. A. Mostofi, J. R. Yates, Y.-S. Lee, I. Souza, D. Vanderbilt, and N. Marzari, wannier90: A tool for obtaining maximally-localised Wannier functions, Comput. Phys. Commun. **178**, 685 (2008).

[30] K. Parlinski, Z. Q. Li, and Y. Kawazoe, First-principles determination of the soft mode in cubic ZrO$_2$, Phys. Rev. Lett. **78**, 4063 (1997).

[31] A. Togo, F. Oba, and I. Tanaka, First-principles calculations of the ferroelastic transition between rutile-type and CaCl$_2$-type SiO$_2$ at high pressures, Phys. Rev. B **78**, 134106 (2008).

[32] C. Zhang, L. Zhang, C. Tang, S. Sanvito, B. Zhou, Z. Jiang, and A. Du, First-principles study of a Mn-doped In$_2$Se$_3$ monolayer: Coexistence of ferromagnetism and ferroelectricity with robust half-metallicity and enhanced polarization, Phys. Rev. B **102**, 134416 (2020).

[33] J. E. Sipe and A. I. Shkrebtii, Second-order optical response in semiconductors, Phys. Rev. B **61**, 5337 (2000).

[34] J. Ibañez-Azpiroz, S. S. Tsirkin, and I. Souza, *Ab initio* calculation of the shift photocurrent by Wannier interpolation, Phys. Rev. B **97**, 245143 (2018).

[35] H. Wang and X. Qian, Electrically and magnetically switchable nonlinear photocurrent in *PT*-symmetric magnetic topological quantum materials, npj Comput. Mater. **6**, 199 (2020).

[36] H. Chen, M. Ye, N. Zou, B.-L. Gu, Y. Xu, and W. Duan, Basic formulation and first-principles implementation of nonlinear magneto-optical effects, Phys. Rev. B **105**, 075123 (2022).

[37] C. Wang, Y. Gao, and D. Xiao, Intrinsic nonlinear Hall effect in antiferromagnetic tetragonal CuMnAs, Phys. Rev. Lett. **127**, 277201 (2021).

[38] Y. Gao and D. Xiao, Nonreciprocal directional dichroism induced by the quantum metric dipole, Phys. Rev. Lett. **122**, 227402 (2019).

[39] J. Ahn, G.-Y. Guo, and N. Nagaosa, Low-frequency divergence and quantum geometry of the bulk photovoltaic effect in topological semimetals, Phys. Rev. X **10**, 041041 (2020).

[40] J. L. P. Hughes and J. E. Sipe, Calculation of second-order optical response in semiconductors, Phys. Rev. B **53**, 10751 (1996).

[41] C. Aversa and J. E. Sipe, Nonlinear optical susceptibilities of semiconductors: Results with a length-gauge analysis, Phys. Rev. B **52**, 14636 (1995).

[42] W. Song, G.-Y. Guo, S. Huang, L. Yang, and L. Yang, First-principles studies of second-order nonlinear optical properties of organic-inorganic hybrid halide perovskites, Phys. Rev. Appl. **13**, 014052 (2020).

[43] H. Wang and X. Qian, Giant optical second harmonic generation in two-dimensional multiferroics, Nano Lett. **17**, 5027 (2017).

[44] B. A. Bernevig, T. L. Hughes, and S.-C. Zhang, Quantum spin Hall effect and topological phase transition in HgTe quantum wells, Science **314**, 1757 (2006).

[45] H. Xu, J. Zhou, and J. Li, Light-induced quantum anomalous Hall effect on the 2D surfaces of 3D topological insulators, Adv. Sci. **8**, 2101508 (2021).

[46] M. N. Chen, W. Su, M. X. Deng, J. Ruan, W. Luo, D. X. Shao, L. Sheng, and D. Y. Xing, Photoinduced topological phase transition and spin polarization in a two-dimensional topological insulator, Phys. Rev. B **94**, 205429 (2016).

[47] D. Sinha, Spin texture of an irradiated warped topological insulator surface, Europhys. Lett. **115**, 37003 (2016).

[48] M. Rodriguez-Vega, M. Vogl, and G. A. Fiete, Low-frequency and moiré–floquet engineering: A review, Ann. Phys. **435**, 168434 (2021).

[49] A. Eckardt and E. Anisimovas, High-frequency approximation for periodically driven quantum systems from a Floquet-space perspective, New J. Phys. **17**, 093039 (2015).

[50] See Supplemental Material at http://link.aps.org/supplemental/10.1103/PhysRevB.109.125101 for van Vleck expansion, Floquet band engineering on the BHZ model, dynamic and thermal

stability of monolayer BiSb, electronic structure of BiSb monolayer, BPVE under Floquet engineering, and SHG under Floquet engineering.

[51] V. K. Kozin, I. V. Iorsh, O. V. Kibis, and I. A. Shelykh, Quantum ring with the Rashba spin-orbit interaction in the regime of strong light-matter coupling, Phys. Rev. B **97**, 155434 (2018).

[52] G. De La Flor, D. Orobengoa, R. A. Evarestov, Y. E. Kitaev, E. Tasci, and M. I. Aroyo, The site-symmetry induced representations of layer groups on the Bilbao Crystallographic Server, J. Appl. Crystallogr. **52**, 1214 (2019).

[53] S. Singh and A. H. Romero, Giant tunable Rashba spin splitting in a two-dimensional BiSb monolayer and in BiSb/AlN heterostructures, Phys. Rev. B **95**, 165444 (2017).

[54] Z. Xu, W. Duan, and Y. Xu, Controllable chirality and band gap of quantum anomalous Hall insulators, Nano Lett. **23**, 305 (2023).

[55] C. Zhang, H. Pi, L. Zhou, S. Li, J. Zhou, A. Du, and H. Weng, Switchable topological phase transition and nonlinear optical properties in a ReC$_2$H monolayer, Phys. Rev. B **105**, 245108 (2022).

[56] L. Wu, S. Patankar, T. Morimoto, N. L. Nair, E. Thewalt, A. Little, J. G. Analytis, J. E. Moore, and J. Orenstein, Giant anisotropic nonlinear optical response in transition metal monopnictide Weyl semimetals, Nat. Phys. **13**, 350 (2017).

[57] L. Z. Tan and A. M. Rappe, Enhancement of the bulk photovoltaic effect in topological insulators, Phys. Rev. Lett. **116**, 237402 (2016).

[58] J.-Y. Shan, M. Ye, S. Lee, J.-G. Park, L. Balents, and D. Hsieh, Giant modulation of optical nonlinearity by Floquet engineering, Nature (London) **600**, 235 (2021).

[59] W. Song, R. Fei, and L. Yang, Nonreciprocal second-harmonic generation in few-layer chromium triiodide, Phys. Rev. B **102**, 045411 (2020).

[60] S. Bergfeld and W. Daum, Second-harmonic generation in GaAs: Experiment versus theoretical predictions of χxyz2, Phys. Rev. Lett. **90**, 036801 (2003).

[61] H. P. Wagner, M. Kühnelt, W. Langbein, and J. M. Hvam, Dispersion of the second-order nonlinear susceptibility in ZnTe, ZnSe, and ZnS, Phys. Rev. B **58**, 10494 (1998).

[62] R. C. Miller, Optical harmonic generation in single crystal BaTiO$_3$, Phys. Rev. **134**, A1313 (1964).

[63] E. J. Sie, J. W. McIver, Y.-H. Lee, L. Fu, J. Kong, and N. Gedik, Valley-selective optical Stark effect in monolayer WS$_2$, Nat. Mater. **14**, 290 (2015).

[64] J. W. McIver, B. Schulte, F.-U. Stein, T. Matsuyama, G. Jotzu, G. Meier, and A. Cavalleri, Light-induced anomalous Hall effect in graphene, Nat. Phys. **16**, 38 (2020).

[65] U. De Giovannini, H. Hübener, and A. Rubio, Monitoring electron-photon dressing in WSe$_2$, Nano Lett. **16**, 7993 (2016).